Mn_3O_4/ZnO-Al_2O_3-CeO_2 mixed oxide catalyst derived from Mn-doped Zn-(Al/Ce)-LDHs: efficient visible light photodegradation of clofibric acid in water

Fatima Zahra Janani, Habiba Khiar, Nawal Taoufik, Mhamed Sadiq, Lidia Favier, Abdelrahman Osama Ezzat, Alaaeddine Elhalil, Noureddine Barka

$Mn_3O_4/ZnO-Al_2O_3-CeO_2$ mixed oxides catalyst derived from Mn doped Zn-(Al/Ce)-LDHs: Efficient visible light photodegradation of clofibric acid in water

Fatima Zahra JANANI [1], Habiba Khiar [1], Nawal Taoufik [1], Mhamed Sadiq [1], Lidia Favier [2], Abdelrahman Osama EZZAT [3], Alaâeddine Elhalil [4], Noureddine BARKA [1,*]

[1] Sultan Moulay Slimane University of Beni Mellal, Multidisciplinary Research and Innovation Laboratory, FP Khouribga, BP.145, 2500 Khouribga, Morocco.

[2] Univ Rennes, Ecole Nationale Supérieure de Chimie de Rennes, CNRS, ISCR-UMR 6226, F-35000 Rennes, France.

[3] Department of Chemistry, College of Sciences, King Saud University, Riyadh 11451, Saudi Arabia.

[4] Laboratory of Process and Environmental Engineering, Higher School of Technology, Hassan II University of Casablanca, Morocco.

[*] Corresponding author: barkanoureddine@yahoo.fr

Abstract

$Mn_3O_4/ZnO-Al_2O_3-CeO_2$ catalyst was synthesized through a solid-state process from 3% Mn-doped Zn-(Al/Ce) layered double hydroxide structure. Detailed structural and optical characterization using XRD, FTIR, UV–visible DRS and TEM was conducted. By investigating clofibric acid (CA) degradation in aqueous solution, $Mn_3O_4/ZnO-Al_2O_3-CeO_2$ photocatalytic activity was evaluated. The results show that the heterostructure mixed oxides catalyst has excellent CA photodegradation performance. Further, the characterization reveals that such photocatalytic efficiency can be attributed to two facts that are summarized in the optical properties and the synergic effect between Mn and Ce elements. The sample demonstrated a narrow band gap of 2.34 eV based on DRS. According to the experimental results of the photodegradation, after 120 minutes of irradiation, the photocatalyst exhibited the highest photocatalytic activity, with a degradation efficiency of 93.6 %. Optimization outcomes indicated that maximum degradation efficiency was attained under the following optimum conditions: catalyst dose of 0.3 g/L, initial dye concentration of 20 mg/L, pH 3.86 and 120 min of reaction time. The quenching test demonstrates that photogenerated electrons and superoxide radicals are the most powerful reactive species. The catalyst could be useful in decreasing the photogenerated charges recombination,

which offers more redox cycles simultaneously during the catalytic process. The strong Ce-Mn interaction and the formation of their different oxidation states offer a high degradation efficiency by facilitating electron-hole transfer. The introduction of Mn_3O_4 in the catalyst can effectively improve the visible absorption properties, which are beneficial in the photocatalytic process by reaching a high catalytic efficiency at a low cost.

Keywords: Mixed oxides; Ce-Mn synergic effect; Visible light photocatalysis; Clofibric acid.

1. Introduction

Emergent molecules like clofibric acid (CA) have been widely used in pharmaceutical formulations. CA is a lipid-lowering agent (Ajala et al. 2022) that reacts against excess cholesterol and reduces blood lipid levels (Aydın et al. 2022). However, CA has a potentially toxic effect on the aquatic environment. Its existence and prolonged accumulation in the ecosystem could pose a major threat to human health (Wu et al. 2022)(Korkmaz et al. 2022). CA is considered one of the most commonly detected emergent molecules in surface water (Ighalo et al. 2020). In 2019, research performed by Chafi et al. (Chafi et al. 2022) reported the presence of CA at about 500 ng/L at rivers in Rabat, Morocco. The observation remains the same for the African water resources (Shehu et al. 2022). Indeed, Silori et al. (Silori et al. 2022) confirmed the presence of CA in these waters in their respective studies. Robelo et al. (Rebelo et al. 2020) indicated the presence of a high amount of CA in different wastewater areas.

Due to its robust structure and immunity to microbial deterioration, CA is challenging to the removal using traditional wastewater treatment (Wu et al. 2022)(Shi et al. 2022). As a consequence, CA has a very extended survival period in the environment possibly up to 21 years (Reza et al. 2014). Furthermore, CA polarity prevents it from being readily absorbed in significant quantities by soil, despite the fact that it easily reaches groundwater or surface waters (Beausse 2004). In order to protect the public's health, more focus has been paid to the development of effective technologies for removing CA from the environment. Photocatalytic process is currently the most effective way to treat wastewater that is rich in contaminants similar to CA (Iqbal et al. 2022). Photodegradation has recently become one of the most promising techniques because it may effectively decompose more kinds of contaminant while also employing a low-cost and efficient process owing to their high oxidation capacity, strong stability, low toxicity, high flexibility, and cost-effectiveness.

Despite its advantages, the recombination behavior of the photogenerated electron-hole pairs during the photocatalytic reaction remains the most hindrance of conventional catalysts (Akir et al. 2017),(Ma et al. 2024). As a result, potential and effective catalysts have been the most important materials for CA oxidation. Several research groups are interested in developing novel catalysts like mixed oxides with low cost and high photocatalytic activity. Mixed metal oxides derived from LDHs materials have been recognized as one of the most effective catalysts for emergent molecule degradation, owing to their higher thermal stability, optical properties, and reusability behavior (Taoufik et al. 2022). Early studies have verified their catalytic performance toward emergent molecules degradation by using bar or doped ZnO oxides such as Ca/ZnO, Mg/ZnO and M-ZnO/CeO_2 where M is Ag or Au (Elhalil et al. 2018a)(Elhalil et al. 2018b)(Liang et al. 2020). Catalysts based on ZnO demonstrated their efficacy against certain kinds of pollutants, like saturated fatty acids, dyes and heavy metals. Furthermore, studies confirmed that combining ZnO with other transition metal oxides can significantly improve its catalytic performance (Janani et al. 2022). In the meanwhile, a number of studies have looked into the use of combination catalysts, such as ZnO and CeO_2, in the photo-degradation of organic contaminants. Due to the heterojunction between the two catalysts, which successfully reduced the recombination of photogenerated charges, these examples showed notable photocatalytic efficacies. Among these instances is the assessment of Cerrato et al. (Cerrato et al. 2022), which verified the excellent photocatalytic activity of CeO_2-ZnO heterojunction impregnated with Cu_2O for the oxidation of tolyltriazole. The improved performance was attributed to the reduced photo-excited electron recombination. Indeed, thanks to their easily achievable Ce^{4+}/Ce^{3+} redox couple (Seo et al. 2021), the recombination of photo-produced charges was reduced. For example, Lin et al. (Lin et al. 2021) reported excellent photocatalytic CA degradation by g-C_3N_4/CeO_2. The obtained results due to the availability of transfer of charge carriers between the g-C_3N_4 and CeO_2 heterojunction. Chaudhari et al. (Chaudhari et al. 2021) evaluated also the catalytic degradation of diclofenac by a catalyst based on CeO_2 and the result demonstrates better photocatalytic activity due to improved charge separation. Typical mixed metal oxides including, Ce-doped Zn/Al (Janani et al. 2021), Mn-Ce-Al-LDO (Zhao et al. 2019) etc., also being investigated for pollutant degradation by different researchers, on account of the high potential of these catalysts towards the contaminants. Additionally, the introduction of CeO_2 in LDHs structures demonstrates the improvement in catalytic performances toward several pollutants (Janani et al. 2021). In general, the advantage of

mixed metal oxides derived from LDHs structures would be their facile manipulation through low cost and eco-friendly approaches. Peculiar photocatalytic performances can be reached by efficient visible light absorption, which provides a performance with high quantum yields and low cost (Wang et al. 2024), (Cheng et al. 2023).

The combination of various redox cycles in the same catalyst has also received attention in order to prevent photogenerated pairs recombination. Wan et al. (Wan et al. 2022) demonstrated that the presence of Mn^{4+}/Mn^{3+} and Ce^{4+}/Ce^{3+} redox couples is beneficial for chlorobenzene oxidation because the simple interaction (Ce^{4+}/Ce^{3+} Mn^{4+}/Mn^{3+}) generates oxygen vacancies on the semi-conductor surface. Therefore, a mixture of ZnO, CeO_2, and MnO_X mixed oxide optimization with appropriate morphology, absorption capacity, and different metal oxidation states would be an effective strategy to develop new catalysts. On the other hand, the correlations between structure design, optical properties, and photocatalytic efficiency also merit more attention. The Mn introduction into Zn-based LDHs greatly improves visible light absorption, avoids photogenerated charge recombination by band offset charge transfer (Binas et al. 2019). Together, the mentioned properties provide excellent photocatalytic performance. However, it has not been reported that Zn-Al-Ce-based LDHs loaded with Mn are used as catalysts in the photodegradation process.

In this work, a $Mn_3O_4/ZnO\text{-}Al_2O_3\text{-}CeO_2$ catalyst was synthesized. The produced catalysts were tested for their ability to degrade CA when exposed to visible light, and they were further examined by XRD, TEM, FTIR, and UV-visible diffuse reflectance technique analysis. The main scope of this study is: i) to obtain $Mn_3O_4/ZnO\text{-}Al_2O_3\text{-}CeO_2$ catalyst with satisfactory catalytic performance and alternatives for typical emergent molecular decomposition; ii) to display new insight regarding the possible influence of Mn incorporation on the structure and activity behavior correlations as well as optical properties improvement for CA photodegradation.

2. Material and methods

2.1. Materials

Analytical-grade chemicals were employed in this study; $Zn(NO_3)_2.6H_2O$ (purity ≥ 99), $Al(NO_3)_3.9H_2O$ (≥ 98), $Ce(NO_3)_3.6H_2O$ (≥ 99%), Na_2CO_3 (≥ 99%), $Mn(NO_3)_2.6H_2O$ (≥ 99.5%), NaOH (≥ 99%), HCl (≥ 37%), and CA (≥ 95%) have been provided by Sigma-Aldrich (Germany). Bidistilled water was used all over this study.

2.2. Catalysts preparation

2.2.1. Synthesis of LDHs and their derived material

The pristine LDHs sample was synthesized through a simple co-precipitation approach (Janani et al. 2021). In 200 mL of deionized water, corresponding amounts of $Zn(NO_3)_2.6H_2O$ and $Al(NO_3)_3.9H_2O$ were dissolved using a Zn/Al molar ratio of 3. Following that, 50 mL of sodium carbonate solution was added to the metal ions solution. The pH of the mixture was then fixed to 8.5 using a NaOH solution. The combined mixture was stirred continuously for 4 hours before being put into a stainless autoclave for 16 hours hydrothermal treatment at 75 °C. The white precipitate was then purified until it achieved a neutral pH solution, and it was then dried for 24 hours at 100°C. The generated substance was finely powdered and kept in test bottles for further use. In a tube furnace, the formed product was calcined at 500°C for 6 hours.

2.2.2. Synthesis of $ZnO\text{-}Al_2O_3\text{-}CeO_2$ and $Mn_3O_4/ZnO\text{-}Al_2O_3\text{-}CeO_2$

The substituted sample was synthesized through the same approach and at the same condition by substituting 10% of Al with Ce, and then the yellow precipitate was calcined at 500°C. The obtained samples were labeled $ZnO\text{-}Al_2O_3$ and $ZnO\text{-}Al_2O_3\text{-}CeO_2$.

The doped catalyst was prepared by solid-state impregnation of pristine Zn-(Al/Ce) with 3% of Mn. The preparation of the sample was performed as follows: Appropriate amounts of the prepared pristine LDHs (Zn-Al/Ce-LDHs) and $Mn(NO_3)_2.6H_2O$ were finely grounded. Then, the obtained mixture was calcined in the same condition of the pristine LDHs samples. The obtained product was labeled $Mn_3O_4/ZnO\text{-}Al_2O_3\text{-}CeO_2$.

2.3. Characterization of the prepared catalysts

Using a Malvern Panalytical Empyrean with CuK radiation, X-ray diffraction patterns of the samples from 7 to 70 were recorded. Highscore software was used to examine the phase indexation. The FullProf program was employed to determine the cell parameters, and Scherrer's equation was used to estimate the size of the crystallite [42]. Transmission electron microscope (TECNAIG2 12 TWIN) operating at an accelerating voltage of 120 kV was used to study the morphology of the materials. A Perkin Elmer FTIR2000 spectrophotometer was used to collect Fourier transform infrared spectra. Room temperature UV-visible diffuse reflectance spectra of the materials were obtained using a Lambda 1050 UV/Vis/NIR spectrometer with a 150 mm

integrating sphere. The spectra were used to calculate the photocatalysts' band gap energy. Drawing lines tangent to the Kubelka-Munk function plots of the resulting spectra, assuming the permitted direct transition, was then conducted to derive the band gap (Eg) value (Dias et al. 2020). The following equations were used to calculate the valence band energy EVB and the conduction band energy ECB (Abdi et al. 2020)(Shan et al. 2021):

$$E_{CB} = \chi - E_e - 0.5E_g \quad (1)$$

$$E_{VB} = E_{CB} + E_g \quad (2)$$

where χ denotes the catalyst's absolute electronegativity and Ee represents the free electron energy vs. hydrogen, which rounds out to 4.5.

2.4. Photocatalytic degradation experiment

A 250 W Halide lamp (λ from 350 to 700 nm) that emit visible light was used to evaluated the catalysts' photocatalytic performance. In order to prevent the lamp from overheating, water circulation in a quartz double jacket was used to maintain the ambient temperature of the using solution constant. In each experiment, 800 mL of CA aqueous solution and 20 mg/L of catalyst powder were combined in the catalytic reactor. The mixture was magnetically stirred for 60 min in the dark to reach adsorption/desorption equilibrium prior to the photocatalytic reaction. After that, the irradiation was started, and the mixture was irradiated on the top and was stirred under continuous oxygen flow for 180 min. In order to confirm the reached photocatalytic performances of the used catalyst, the photocatalytic activity of the prepared catalyst was compared to commercial P25 TiO_2, which it was irradiated under UV irradiation (UV mercury lamp: 400w) and at the identical conditions (m=50mg, C_0=20mg/L and pH=3.86). A METASH UV-vis spectrophotometer operating at a wavelength of 278 nm was used to measure the concentration of CA at predetermined time intervals.

The adsorbed amount Q_{ads} (mg/g) and the degradation efficiency (D.E.%) were calculated according to the following equations:

$$Q_{ads} = (C_0\text{-}C_t)*(V/m) \quad (3)$$

$$D.E.\% = 100*(C_0\text{-}C_t)/C_0 \quad (4)$$

where C_0 and C_t signify the CA concentrations before and after adsorption (mg/L) and R (g/L) refers to the mass of the Mn_3O_4/ZnO-Al_2O_3-CeO_2 catalyst per liter of aqueous solution.

Using the pseudo-first-order kinetics model, the photocatalytic degradation was expressed and the kinetic constant was assessed. The equation for the model can be explained as follows:

$$Ln(C_0/C_t) = k_{ap}\, t \quad (5)$$

where the k_{ap} is the apparent rate constant (min^{-1}).

Furthermore, the operation parameters were modified to evaluate the catalytic performances under different conditions. The solution's initial pH was ranged from 3.86 to 9.5 at C_0=50mg/L and m=20mg/L, and the starting CA concentration was ranged from 25 to 50 mg/L at pH of 3.86 and m=20mg/L. The scavenging test was performed to identify the reactive species responsible for the CA photodegradation by adding $AgNO_3$ (1 mM), EDTA (1 mM), ethanol (1 mM), or ascorbic acid (10 mM) as trapping agents for $\bar{e}$, h^+,·OH, and $O_2^{\cdot -}$, respectively. This test was explored at the optimal condition by using 50mg/L of CA, pH 3.86 and catalyst dose of 20 mg/L. The photostability and reusability of the used catalyst were established after 3 cycles of photocatalytic degradation testing under identical conditions. After each experiment, the catalyst powder was dried at 100°C and was then reused in another CA aqueous solution degradation reaction.

3. Results and discussion

3.1. Catalysts characterization

3.1.1. X-ray diffraction

Figure 1 depicts the various XRD patterns obtained from the different samples. According to the result, the pristine Zn-Al and pristine Zn-(Al/Ce) exhibit characteristic patterns of lamellar structures. The main reflection corresponds to a hydrotalcite like structure for both samples, and it is clearly seen that the sample substituted by Ce conserves its lamellar structure with the presence of an additional peak at the 2θ value between 27° and 30° assigned to the CeO_2/Ce_2O_3 impurities (JCPDS No. 81-0792) (Hussain et al. 2016)(Nagendran et al. 2018). The characteristic peaks of the pristine Zn-Al sample are located at 2θ related to (003), (006), (012), (015), (018), (1010), (0111), (110), and (113) planes of layered double hydroxide structure (JCPDS No. 38–0486) (Olfs et al. 2009). Using FullProf software, the reflection peaks were fitted to a hexagonal phase with rhombohedral 3R symmetry and space group P6/mmm. The cell parameters, volume, and

interlayer distance for the prepared pristine LDHs are calculated. The cell parameters and volume cell are proportionally dependent on the ionic radii. A slight increase in these cell parameters and a remarkable change in peak location result from Al being substituted with Ce, whose ionic radius is larger than Al (1.01 and 0.54 Å, respectively). With an increase in metal radius, which is directly related to the angle 2θ, the d value rises (7.55 Å and 9.3 Å for pristines Zn-Al and Zn-(Al/Ce), respectively). As a result, θ values decrease as the interlayer distance increases, according to the Bragg equation: $2d\sin\theta = n\lambda$. This is consistent with the peak position shifting to the lower 2 degrees.

Table 1 indicates a slightly difference in parameters a, c, and volume cell with incorporation of Ce in the LDHs matrix. The interplanar spacing increased steadily with increasing average radii of metallic cations, which depends directly on the angle q in accordance with Bragg's equation. A considerable decrease of parameter c was observed with increase in Ce content; this is due to the low affinity of intercalation of carbonate. The same tendency was observed in the crystallite size, which were significantly dependent on the unit cell.

Table 1: Calculated unit cell parameters, crystal sizes and volume cell of the calcined LDHs materials.

Catalyst	Lattice parameters (A˚)		Cell volume ($A^{\circ 3}$)	Crystallite size (A˚)
	a	c		
Zn-Al-CO_3	3.069	22.613	184.451	185.12
Zn-Al-Ce5%-CO_3	3.071	22.723	185.7	223.4
Zn-Al-Ce10%-CO_3	7.568	22.572	1119.73	170.2

The patterns clearly show that the lamellar structure has been completely distorted following calcination. The diffraction peaks correspond to ZnO were observed in calcined samples. Some additional peaks for the substituted matrix, corresponding to the CeO_2 and Ce_2O_3 cubic fluorite structures with coincident primary reflections to the planes (111), were also observed (220) (Yang et al. 2014)(Nagendran et al. 2018)(Hussain et al. 2016). No further characteristic reflections correspond to Al_2O_3, confirming the amorphous structure of this oxide (ZHANG et al. 2016). The characteristic peaks attributed to ZnO were indexed at (100), (002), (101), (102), (110),

(103), (200), (112) and (201) planes, corresponding to 2θ of 31.74°, 34.4°, 36.22°, 47.51°, 56.59°, 62.85°, 66.35°, 67.93° and 69.09°, respectively (JCPDS Card No.00-001-1127) (Sahoo et al. 2015). For the Mn doped catalyst, remarkable reflection peaks appeared at 2θ of 28.42° and 47.6° indexed to the (112) and (220) planes, and it is seen that the diffraction peaks have shifted to the lower 2θ. These peaks correspond to the formation of Mn_3O_4 in the sample with relatively weak peak intensities, suggesting that the Mn_3O_4 oxide is well dispersed in the ZnO-Al_2O_3-CeO_2 matrix surface (Velu et al. 1999). The presence of Mn_3O_4 was confirmed by the peak's intensity rising after catalyst doping, which means that the Mn metal was successfully introduced into the lattice. In the doped catalyst, it is worthy to mention that the crystallite size of the heterostructure was systematically increased by Mn doping, which has a value of 28.7 nm, 3.016 nm, and 2,19 nm for Mn_3O_4/ ZnO-Al_2O_3-CeO_2, ZnO-Al_2O_3 and ZnO-Al_2O_3-CeO_2, respectively, indicating that a small Mn content affects the crystallite size of the sample.

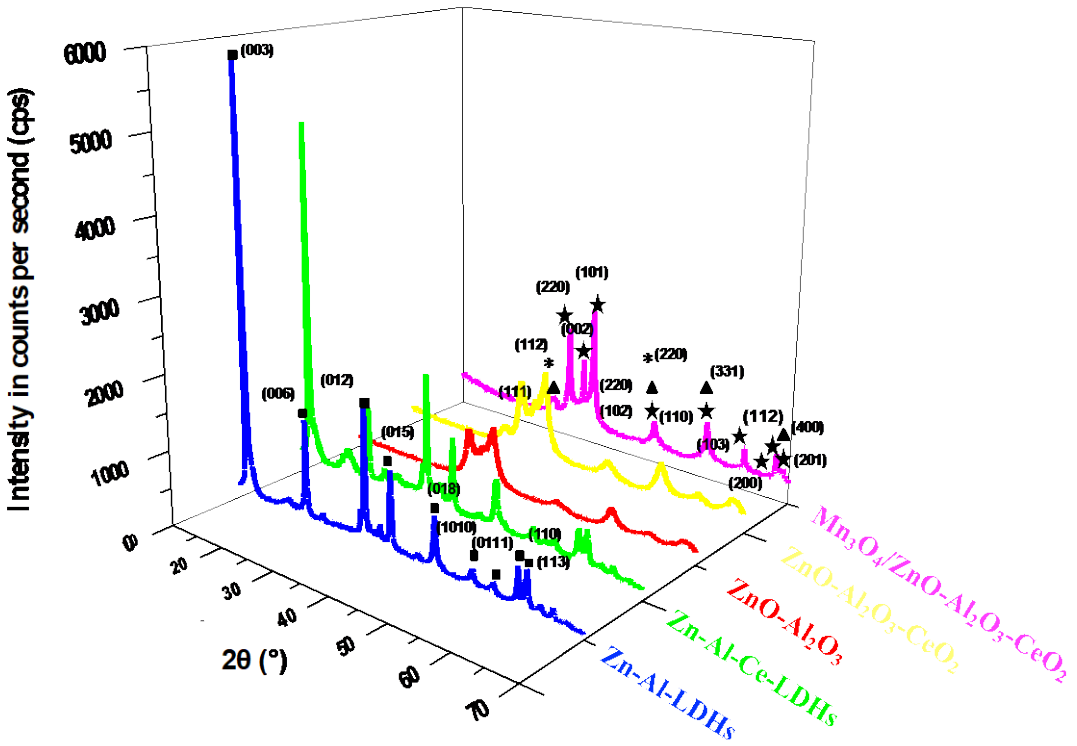

Fig.1. XRD patterns of different samples (▪pristine LDHs; ▪ZnO; ▲CeO_2/Ce_2O_3; ⁎Mn_3O_4).

3.1.2. Fourier transform infrared spectra

Fig.2 presents the FTIR spectra of the materials between 4000 cm^{-1} and 400 cm^{-1}. The spectra of pristine Zn-Al and Zn-(Al/Ce) show a large absorption band between 3500 and 3200 cm^{-1}. This

band can be linked to the hydroxyl group stretching vibration present in the brucitic sheets as well as in the H_2O molecules mainly intercalated in the lamellar space or adsorbed on the material surface. The angular deformation vibration of the intercalated water molecules (H_2O) can be observed at 1600 cm^{-1}. The interlamellar carbonate ions are marked by the asymmetric stretching vibration around 1350-1380 cm^{-1}, outside-plane deformation at 850-880 cm^{-1} and in-plane bending vibration at 670-690 cm^{-1}. Among the characteristic vibrational bands of the pristine LDHs that cover the region between 1000 cm^{-1} and 400 cm^{-1}. The observed bands at around 430 cm^{-1} correspond to O-M-O strain, and the bending vibrations between 670 cm^{-1} and 590 cm^{-1} are linked to M-O elongation vibrations. Even after calcination of pristine LDHs structure, some H_2O molecules from the air were reversibly absorbed on the oxide surfaces during the powder storage. Compared with the synthesized pristine LDHs structure, there was a slight decrease of the metal-oxygen intensity bands. This could be due to the charge distribution in the lamellar medium as a result of the calcination process, as well as the subsequent organization of cations within the sheet.

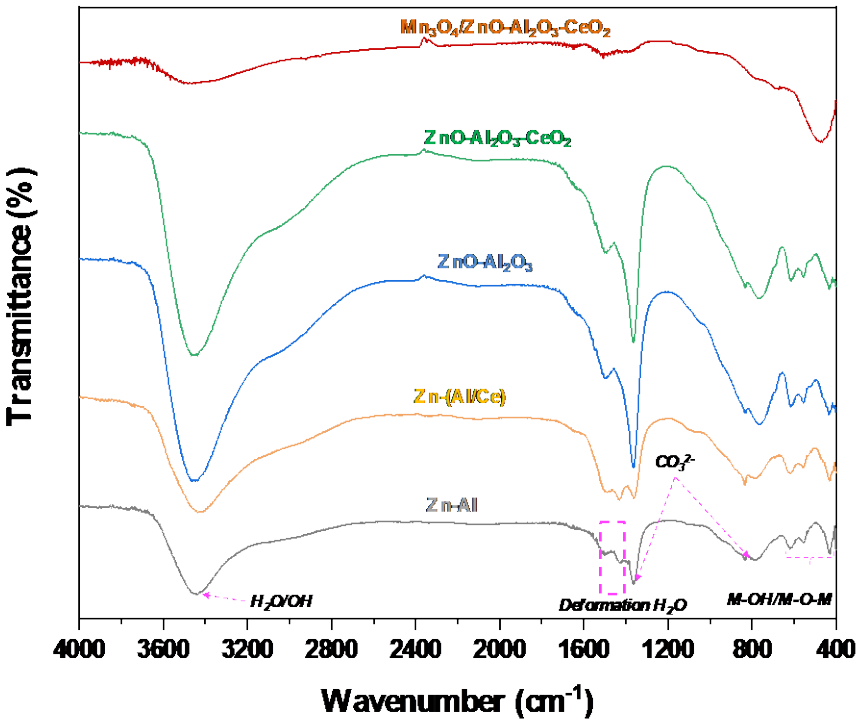

Fig.2. FTIR spectrum of different materials.

3.1.3. Optoelectronic properties

The optical characteristics of catalysts are the key criterion of their photocatalytic activity. The UV-vis diffuse spectra of such mixed metal oxides are depicted in Figure 3. As shown in the spectra, all the catalysts exhibit an intense absorption band in the UV region, dedicated to a charge transfer of M-O. Interestingly, the absorption band intensity underwent a significant change, for which an increased absorption intensity can be clearly observed in the visible region for Mn_3O_4/ZnO-Al_2O_3-CeO_2. Near to 350 nm is the optimal energy absorbed by all samples (UV area). The incorporation of Mn proved to have culminated in a greater capacity for absorption. This highest absorption band intensity of the semi-conductor material is primarily attributed to the synergistic effect between Mn_3O_4 and the ZnO-Al_2O_3-CeO_2 system. It is worthy of mention that UV-vis spectra provide more information related to electron transitions and the oxidation states of the used catalyst (Velu et al. 1999). Thought, the d-d transition in Mn^{2+} and Mn^{3+} can be used to explain visible absorption bands. Weak bands intensity in the 400–600 nm range are ascribed to the Mn^{2+} specie, which is spin- and orbital-forbidden (Velu et al. 1999). The bands detected at the two wavelengths of 500 nm and 610 nm are assigned to the electron transition of 6A1g → 4T2g crystal field transitions of Mn^{2+} (Velu et al. 1999)(Pratt and Coelho 1959)(Kijlstra et al. 1997). Moreover, the observed absorption band at 755 nm corresponds to 5B1g → 5A1g d–d transitions in Mn^{3+}. Since Mn^{2+} and Mn^{3+} can also be present but overlap with the above-described transition, it could be argued that manganese is present based on the absorption bands in the 500–800 nm area (Pratt and Coelho 1959)(Kijlstra et al. 1997). Owing to the presence of these absorption bands, it is expected that the Mn is available in Mn^{2+} and Mn^{3+} oxidation states. Independently of the valence states of Mn, it was obviously assigned the absorption band expansion in the visible area to the Mn incorporation, which presents a band gap of 2.34 eV smaller than those of ZnO-Al_2O_3 and ZnO-Al_2O_3-CeO_2 of 3.14 eV and 3.02 eV, respectively (see Fig.4). As a matter of fact, it is liable to be assumed that the board absorption band of Mn_3O_4/ZnO-Al_2O_3-CeO_2, along with the band capacity stretching to the visible region, could mainly enhance photon absorption and be a viable candidate for boosting the photocatalytic degradation pathway. A remarkable shift was clarified from the results shown in the spectra, after the formation of Mn_3O_4/ZnO-Al_2O_3-CeO_2, the valence band moved up and the conduction band moved down, which is mostly responsible for the band gap reduction. The conduction band of Mn_3O_4/Zn-(Al/Ce)-MMO is located in a more positive position, reaching a value of -0.16 eV (ECB= -0.16 Vs NHE) than that of ZnO-Al_2O_3 (ECB = -0.59 Vs NHE) and ZnO-Al_2O_3-CeO_2 (ECB = -0.52 Vs NHE). For the valance band, it is

also shifted to a smaller value (EVB =2.18 eV) than those obtained for ZnO-Al_2O_3 (EVB = 2.55 eV) and Zn-(Al/Ce)-MMO (EVB =2.5 eV).

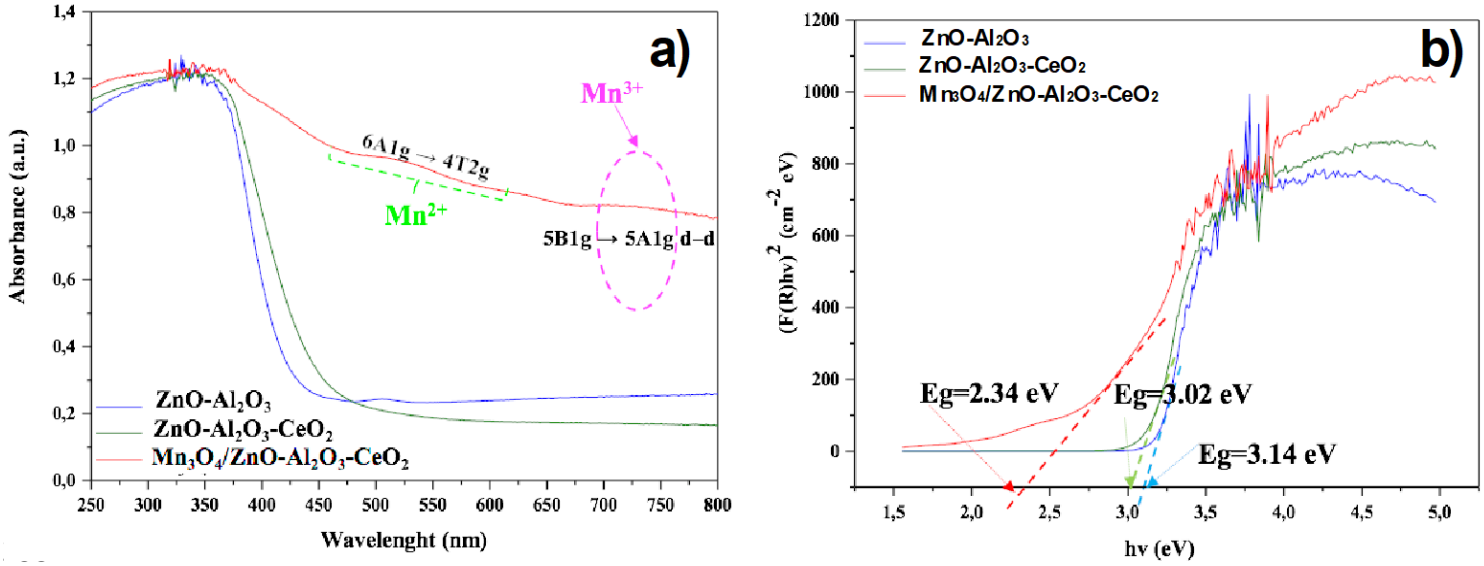

Fig.3. UV–vis DRS for ZnO-Al_2O_3, ZnO-Al_2O_3-CeO_2 and Mn_3O_4/ZnO-Al_2O_3-CeO_2.

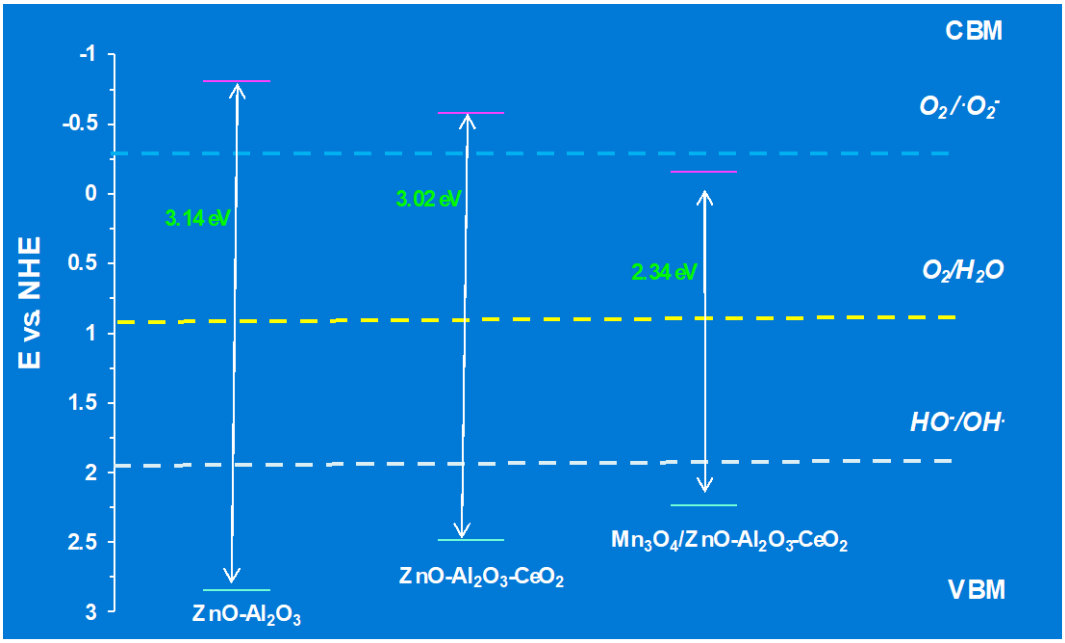

Fig.4. Representation of the band gap edges for ZnO-Al_2O_3; ZnO-Al_2O_3-CeO_2 and Mn_3O_4/ZnO-Al_2O_3-CeO_2.

3.1.4. TEM analysis

Fig.5 shows TEM graphs of the surface morphology of the Mn_3O_4/ZnO-Al_2O_3-CeO_2 catalyst at various magnifications. The figure shows the formation of a dense heterostructure with agglomerated, indistinct grains on the catalyst surface. A disordered structure and the irregular and unshaped forms of the sample were observed, indicating the evolution of mixed oxides with various morphologies. The 'darker diapers' remarked can be linked to the formation of manganese oxide on the sample surface, due to the distribution of segregated Mn particles as oxide on the sample surface. The images also show the formation of a rolled-sheet-like structure. According to reported studies, the CeO_2 nucleation is mainly affected by the presence of Mn like oxides (Wan et al. 2022)(Wu et al. 2011)(Mohan et al. 2012). Manganese oxide excess can also result in rolled morphology that is individually sandwiched (Morales-mendoza et al. 2015). So, the finding suggests that the introduction of the Mn oxides into the system avoids the homogenous distribution of the constituent elements of the system, leading to the formation of rolled-like morphologies. The obtained heterostructure morphology of the mixed metal oxides seems extremely favorable for improving photocatalytic application.

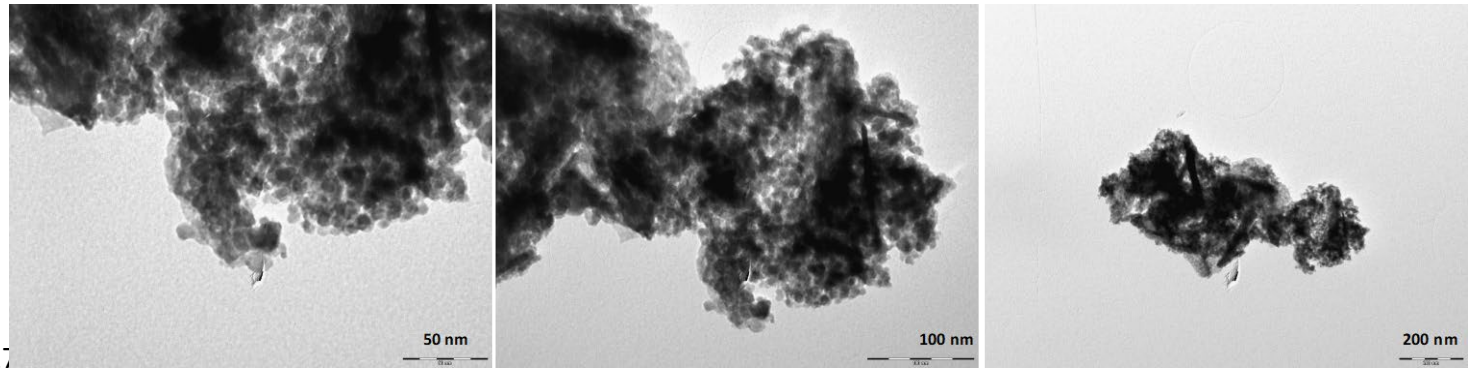

Fig. 5. TEM images of Mn_3O_4/ZnO-Al_2O_3-CeO_2 catalyst.

3.2. Adsorption/Photocatalytic performances

The photocatalytic degradation of CA through the catalysts expressed in term of C/C_0 us function of time is reported in Fig.6. As shown, from the photolysis test, about 20% of CA degradation efficiency was achieved after 120 min, which was negligible compared to that reached in the presence of each used catalyst The Mn_3O_4/ZnO-Al_2O_3-CeO_2 heterostructure shows the highest photocatalytic efficiency compared to ZnO-Al_2O_3, ZnO-Al_2O_3-CeO_2 and commercial TiO_2 catalysts under the conditions. The majority of CA was degraded within 120 min by using

Mn_3O_4/ZnO-Al_2O_3-CeO_2, which exhibits 93.6 % degradation efficiency under visible light irradiation with a constant rate of $2.47*10^{-2}$ min^{-1}. While ZnO-Al_2O_3, Mn_3O_4/ZnO-Al_2O_3-CeO_2 and TiO_2 achieve only 69.91 %; $1.66*10^{-2}$ min^{-1}, 90.36 %; $2.06*10^{-2}$ min^{-1} and 84.68 %; $1.8*10^{-2}$ min^{-1}, respectively. On the other hand, the photocatalytic performance considerably depends on the adsorption behavior of the catalysts. As demonstrated in Fig. 7, there is a high correlation between the adsorbed amounts and the kinetic rate constant of photodegradation. During the photodegradation process, the adsorption behavior is crucial, which will accelerate the photocatalytic reaction. Therefore, based on the UV-vis DRS data that were obtained and the calculated experimental parameters, the highest photocatalytic activity of Mn_3O_4/ZnO-Al_2O_3-CeO_2 is primarily due to the significant adsorption ability of CA onto the surface of catalyst, to the surface morphology, and to the optical characteristics.

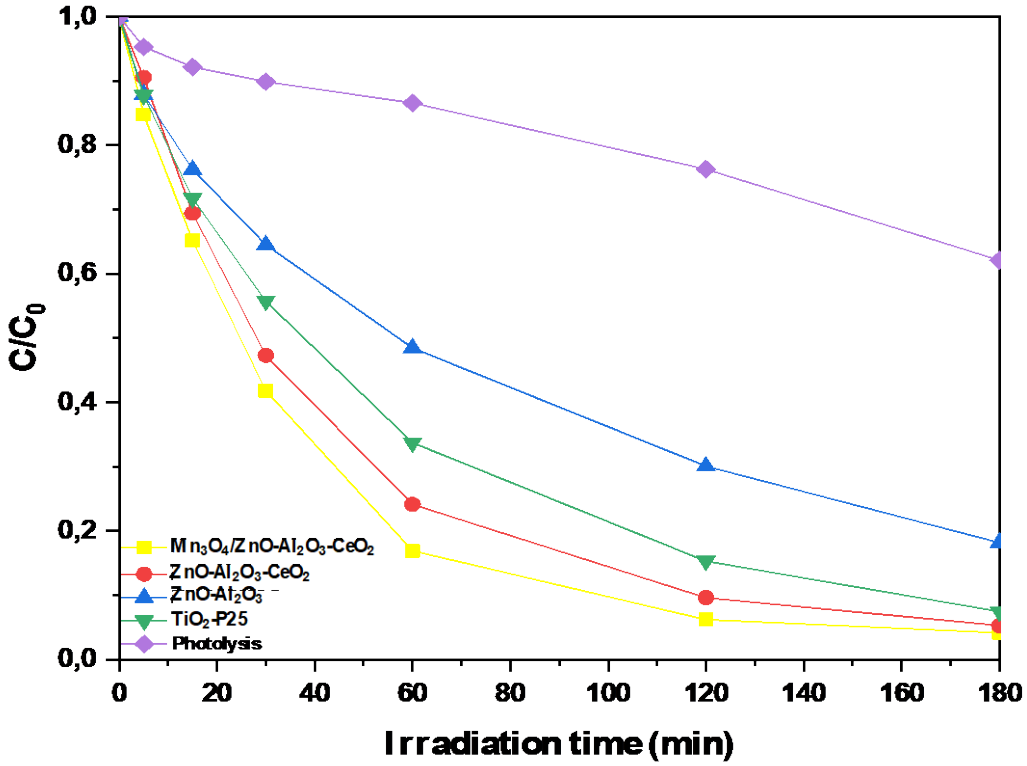

Fig.6. Kinetics of CA photodegradation over catalysts (C_0= 50 mg/L; m= 20 mg/L; pH of solution ~3.86)

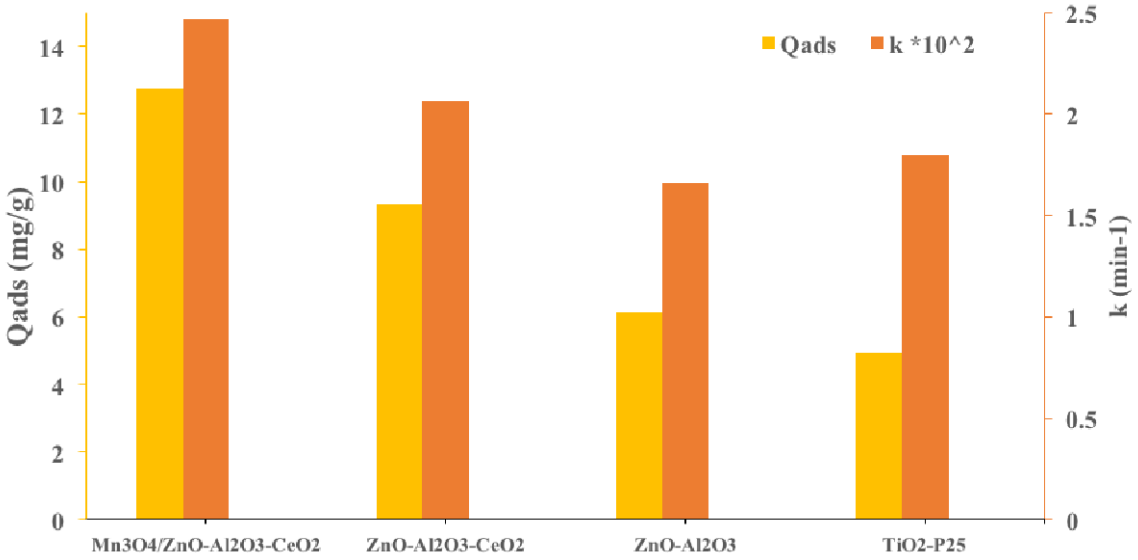

340

341 **Fig.7.** Correlation between degradation rate and adsorbed amounts of CA by different
342 photocatalysts (m= 20 mg/L; C_0= 50 mg/L; pH of the solution ~3.86).

343 **3.2.1. Effect of the initial solution pH**

344 In the photocatalytic process, the pH of the solution is crucial. Fig.8 illustrates the change
345 observed in degradation efficiency of CA by Mn_3O_4/ZnO-Al_2O_3-CeO_2 with the change of initial
346 solution pH. As illustrated in Fig. 9, the photocatalytic activity increased at a natural solution pH
347 of 3.86, dropped when the pH was raised to 7.5, and then slightly increased at pH 9.5. The catalyst
348 exhibits a maximum degradation efficiency in acidic medium achieving 93.6% of efficiency.
349 While 77.01 and 86.06 % for neutral and basic solution, respectively. The apparent rate constant
350 of CA photodegradation at pH of 3.86 is over faster than those at pH 7.5 and 9.5. As known, the
351 catalyst surface is significantly affected by the solution pH, it can be protonated or deprotonated
352 depending on its pH_{PZC}. The catalyst exhibits a pH_{PZC} of 8, which indicates that its surface is
353 positively charged below of this value, and negatively charged above of it. Furthermore, Fig.9 (a)
354 shows the species distribution of CA and its pKa value, which is around 3.18. By increasing pH
355 from 0 to 12, it can be seen that the molecular form fraction reduced while the anionic form fraction
356 increased. According to the experimental data, the higher adsorbed amount was observed at a low
357 pH value and then decreased by increasing the pH of the solution. This outcome might be assigned
358 to the electrostatic interactions between the CA anions and the catalysts protonated surface.
359 Similarly, increasing the pH of CA reduces its adsorption capacity primarily due to repulsion

360 interactions between the negative surface charge and the anionic form fraction of CA in the basic
361 medium (Fig. 9(b)). At a high pH value, more ·OH could be generated through $^{-}$OH groups, which
362 are the powerful oxidants in the photocatalytic process.

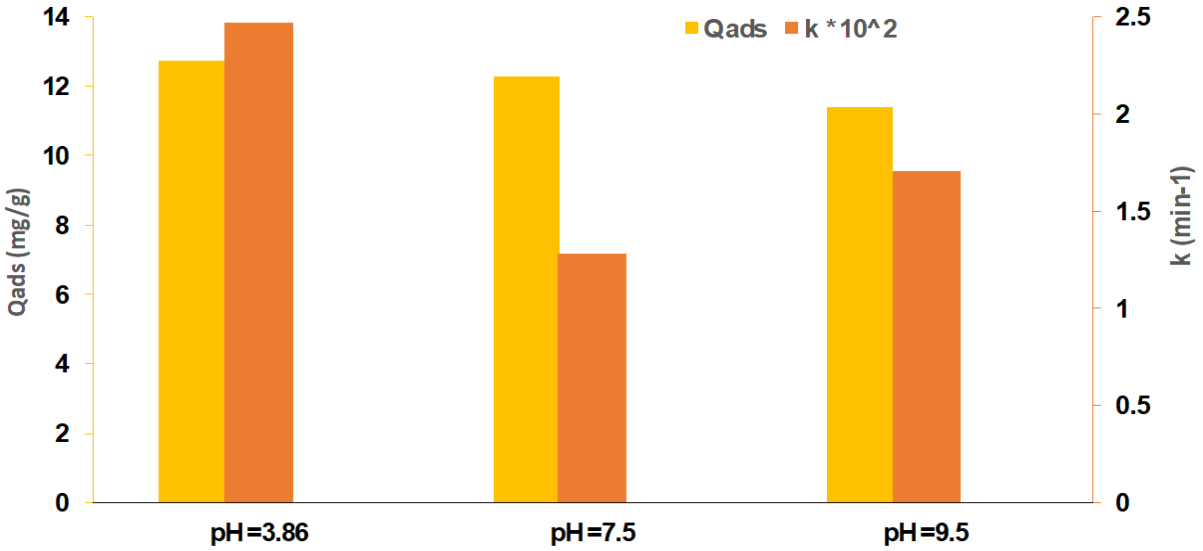

363

364 **Fig.8.** Effect of initial solution pH of CA on its adsorption and degradation efficiency by
365 Mn_3O_4/ZnO-Al_2O_3-CeO_2.

366

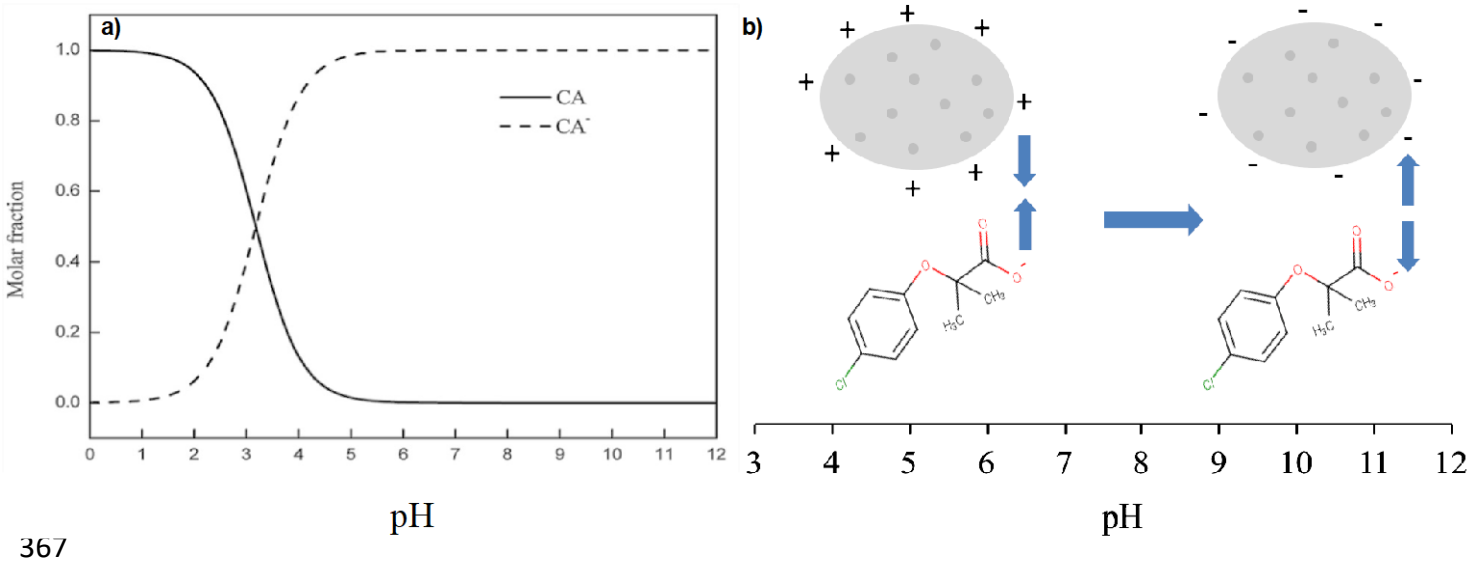

367

368 **Fig.9.** Distribution of dissociation species of CA (a) and the predicted electrostatic interaction
369 between CA and Mn_3O_4/ZnO-Al_2O_3-CeO_2 surface depending pH_{pzc} (b).

3.2.2. Effect of the initial concentration of CAF

Fig.10 shows the kinetics of CA photocatalytic oxidation at varied starting concentrations. The insert of the figure also displays the $\ln(C_0/C)$ against time plot. The data reveals that the initial CA concentration affects the kinetics of degradation. At low concentration, the photodegradation process was very faster in a short time. These results indicated that a significant number of active sites were available at the start of the reaction, increasing the photodegradation rate. The degradation kinetics at different concentration fits considerably the pseudo-first order kinetic model. By increasing starting concentration, the efficiency of CA degradation tends to decline. Therefore, a lower initial CA concentration could increase the performance of CA removal This could be explained by the fact that, as the starting pollutant content rises, more molecules were deposited on the photocatalyst surface. The adsorption of O_2 and ^{-}OH on the catalyst surface reduced as more active sites were filled by the CA molecules, which reduced the amount of radical production. Furthermore, a decline in photon adsorption by the catalyst due to a photon penetration inhibition on its surface leads to a decrease in the generation of reactive species. Thus, the important degradation of a high concentration of CA requires a very efficient catalyst. As a consequence, the synthesized Mn_3O_4/ZnO-Al_2O_3-CeO_2 leads to excellent CA degradation efficiency at high initial concentrations.

In order to make a comparison with other catalysts, Table 1 reports information about several studies regarding the CA degradation in aqueous solutions carried out with different operating conditions. It is necessary to underline that the literature about the degradation of CA by photocatalytic processes using Mn_3O_4/ZnO-Al_2O_3-CeO_2 is not reported. From the Table 1, it is possible to observe that, Mn_3O_4/ZnO-Al_2O_3-CeO_2 employed in our study provide higher performances in CA also after several reuse cycles. A direct comparison between the commercial TiO2-P25 and our system is applicable to show the efficient performance of the used material.

A low dose of the proposed material exhibits excellent photodegradation in a shorter time and for a high concentrations of CA.

The existence of mixed metal oxides based on Mn, Ce, and Zn, which are confirmed for prospective use in the photocatalytic test, may be the reason for the findings. The main properties of the presented catalyst would make the photocatalytic process economically feasible. In addition, none of the analyzed papers reports data about the synthesis, application, stability and reusability of the tested material.

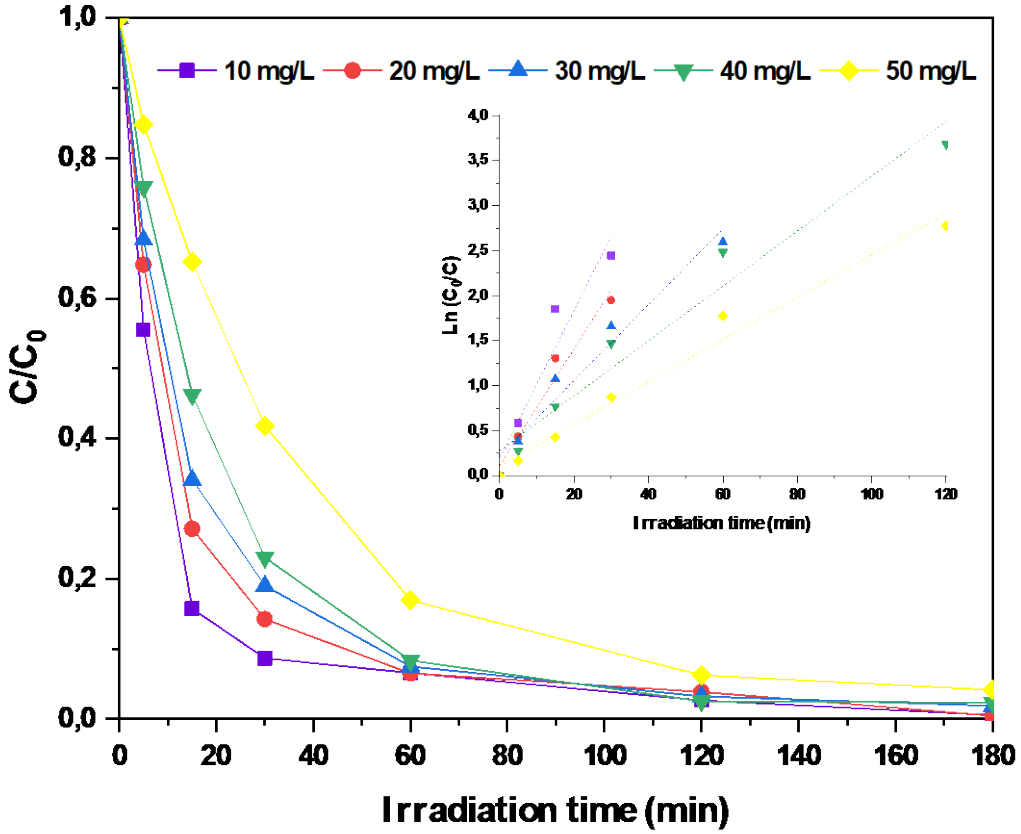

Fig.10. Effect of initial CA concentration on its photocatalytic degradation over Mn_3O_4/ZnO-Al_2O_3-CeO_2 (m=20 mg/L; pH of solution ~3,86).

Table 1. Comparison of the effectiveness of Mn_3O_4/ZnO-Al_2O_3-CeO_2 for CA degradation with published data.

Catalyst	Concentration (mg/L)	Catalyst dose (mg/L)	Ratio (m/C)	pH	Light source	Time (min)	k_{app} (min^{-1}) and D.E (%)	Ref.
g-C_3N_4/P25	2.0	25	12.5	5.3	Sunlight	30	0.039, 85.4	(Chen et al. 2017)
TiO_2	1.5	1000	666.6	5.9	2 UVA lamps	130	0.077, 85	(Favier et al. 2019)
Zn-La mixed oxide	20	500	25	Natural	UV light	90	97	(Sescu et al. 2020)
g-C_3N_4/CeO_2	21.5	500	23.25	4.5	Visible light	60	98.5	(Lin et al. 2021)
Mn_3O_4/Zn-(Al/Ce)-MMO	50	20	0.4	3.86	Visible light	120	0.0247, 93.6	This work

3.2.3. Discussion of photocatalytic mechanism

From the previously discussed results, we assumed that the main reason for the excellent photocatalytic performances toward the degradation of CA can be assigned to two facts: the incorporation of Mn in the system, which extends the absorption intensity to the visible area and enhances the optical characteristics of the produced samples owing to the existence of the two oxidation states of Mn (Mn^{2+} and Mn^{3+}). This is confirmed by UV-vis spectra and the synergic effect between CeO_2 and Mn_3O_4 as reported in the literature (Wan et al. 2022)(Binas et al. 2019)(Morales-mendoza et al. 2015). The presence of mixed oxides promotes CA degradation via a strong synergy between CeO_2 and Mn_3O_4, which promotes (Ce^{4+}/Ce^{3+} Mn^{4+}/Mn^{3+}) redox couples. A brief discussion about the enhanced photocatalytic performance of the Mn_3O_4/ZnO-Al_2O_3-CeO_2 heterostructure is suggested to be as follows: Firstly, it is widely acknowledged that the presence of intermediate photogenerated active species such as electron (ē), holes (h+), superoxide radicals (O2.-) and hydroxyl radicals (.OH) on the exposed surface catalyst is primarily responsible for the photocatalytic reaction (Shang et al. 2019). Fundamentally, electron-hole pairs effectively contribute to the degradation process in the photocatalytic process; the holes (h^+) directly reacted with the organic molecules deposited on the catalyst surface or with the OH^- anion present in an aqueous solution to produce $^{\cdot}OH$ radicals. The photo-induced electrons (ē) are captured through adsorbed O_2 forming $O_2^{\cdot-}$ radicals, which participate in the generation of $OH^{\cdot}$ by a simple reaction with H_2O molecules. The fast rate of photogenerated charges recombination, which prevents the degradation reaction of organic compounds, is the process's fundamental flaw. So, the presence of redox cycles in the catalytic system can significantly improve the carrier's charge separation by avoiding their recombination rate, promoting the favorite migration of electrons to the CB, and producing more holes in the CB. To explore the photocatalytic degradation of the CA mechanism, quenching tests were performed. Fig.11 demonstrates that the photodegradation efficiency decreased from 93.6 % to 64.23, 63.10, 27.9 and 21.7 % after the addition of ethanol, EDTA, ascorbic acid, and $AgNO_3$, respectively. So, based on the obtained date, the photogenerated electrons and superoxide radicals are the most responsible in the photocatalytic degradation reaction of CA. Additionally, the hydroxyl radicals and holes provide a reasonable contribution to the photodegradation of CA.

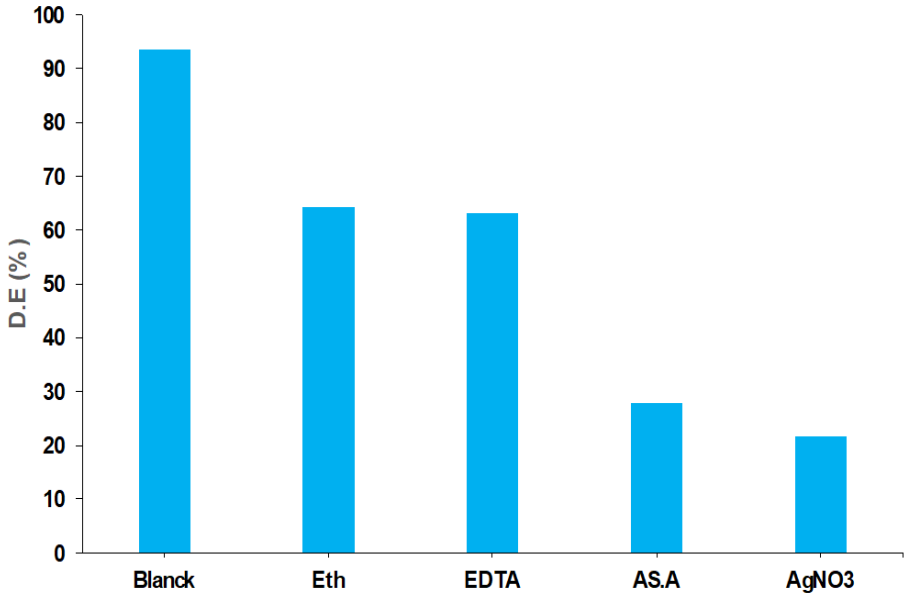

Fig.11: Scavenger reactive species.

In this case, we can propose that the most responsible and powerful active species are photogenerated electrons and that the Mn can exist in a variety of oxidation states (Mn^{+}, Mn^{2+}, Mn^{3+} and Mn^{4+}) owing to the production of $\bar{e}$-h^{+} charges under irradiation. The excitation of the catalyst surface by visible light provides for the transfer of electrons ($\bar{e}$) to the CB, producing deficiency charges like holes (h^{+}) in the VB (Eqt 6), which could oxidize the present species in aqueous solution. According to the band edge position of the catalyst, the creation of $OH^{\cdot}$ species is induced by the holes (Eqt 26). Similarly, the generated electrons reduced the Mn^{x+}, Ce^{x+}, leading to the formation of elements with different valences (Eqts 8,9,10,18,19,20 and 21). In addition, the lifetime of these generated pairs was increased owing to the presence of different couple redox, which provide a high photogenerated charges separation and enhance significantly the catalytic performance of the photocatalyst. The high degradation efficiency could be assigned to the photogenerated $\bar{e}$ capture through Ce^{4+} in 4f level of cerium ion, Mn^{2+}, Mn^{3+} and Mn^{4+} forming Ce^{3+}, Mn^{+}, Mn^{2+} and Mn^{3+}, respectively. These couple redox leads to formation of the intermediate reactive species mainly including $OH^{\cdot}$ (Eqts 11,12,13 and 14), $O_2^{\cdot -}$ (Eqts 15, 22,23,24 and 25), $HOO^{\cdot}$ (Eqt16) and H_2O_2 (Eqt 17 and 27). According to the band position spectra (Fig.5), all of the mentioned reactive species could be produces. As a consequent, the high interaction between Ce and Mn species contribute to reaching a potential photocatalytic efficiency. The proposed reactions pathway is examined as following:

Catalyst surface + hν → $e^- + h^+$ (6)

$Ce^{4+} + Mn^{3+} \rightarrow Ce^{3+} + Mn^{4+}$ (7)

Reduction process: $Mn^{3+} + \bar{e} \rightarrow Mn^{2+}$ (8)

$Mn^{3+} + \bar{e} \rightarrow Mn^{2+}$ (9)

$Mn^{2+} + \bar{e} \rightarrow Mn^{+}$ (10)

$Ce^{4+} + OH^- \rightarrow Ce^{3+} + OH^{\cdot}$ (11)

$Mn^{4+} + OH^- \rightarrow Mn^{3+} + OH^{\cdot}$ (12)

$Mn^{3+} + OH^- \rightarrow Mn^{2+} + OH^{\cdot}$ (13)

$Mn^{2+} + OH^- \rightarrow Mn^{+} + OH^{\cdot}$ (14)

$e^- + O_{2ads} \rightarrow O_2^{\cdot -}$ (15)

$O_2^{\cdot -} + H^+ \rightarrow HOO^{\cdot}$ (16)

$HOO^{\cdot} + H^+ + e^- \rightarrow H_2O_2$ (17)

Oxidation processes: $Ce^{3+} + h^+ \rightarrow * Ce^{4+}$ (18)

$Mn^{+} + h^+ \rightarrow * Mn^{2+}$ (19)

$Mn^{2+} + h^+ \rightarrow * Mn^{3+}$ (20)

$Mn^{3+} + h^+ \rightarrow * Mn^{4+}$ (21)

$Ce^{3+} + O_{2ads} \rightarrow Ce^{4+} + O_2^{\cdot -}$ (22)

$Mn^{+} + O_{2ads} \rightarrow Mn^{2+} + O_2^{\cdot -}$ (23)

$Mn^{2+} + O_{2ads} \rightarrow Mn^{3+} + O_2^{\cdot -}$ (24)

$Mn^{3+} + O_{2ads} \rightarrow Mn^{4+} + O_2^{\cdot -}$ (25)

$OH^- + h^+ \rightarrow OH^{\cdot}$ (26)

$OH^{\cdot} + OH^{\cdot} \rightarrow H_2O_2$ (27)

CA + Reactive species → Byproducts+$HO^{\cdot}$ → $CO_2 + H_2O$ (28)

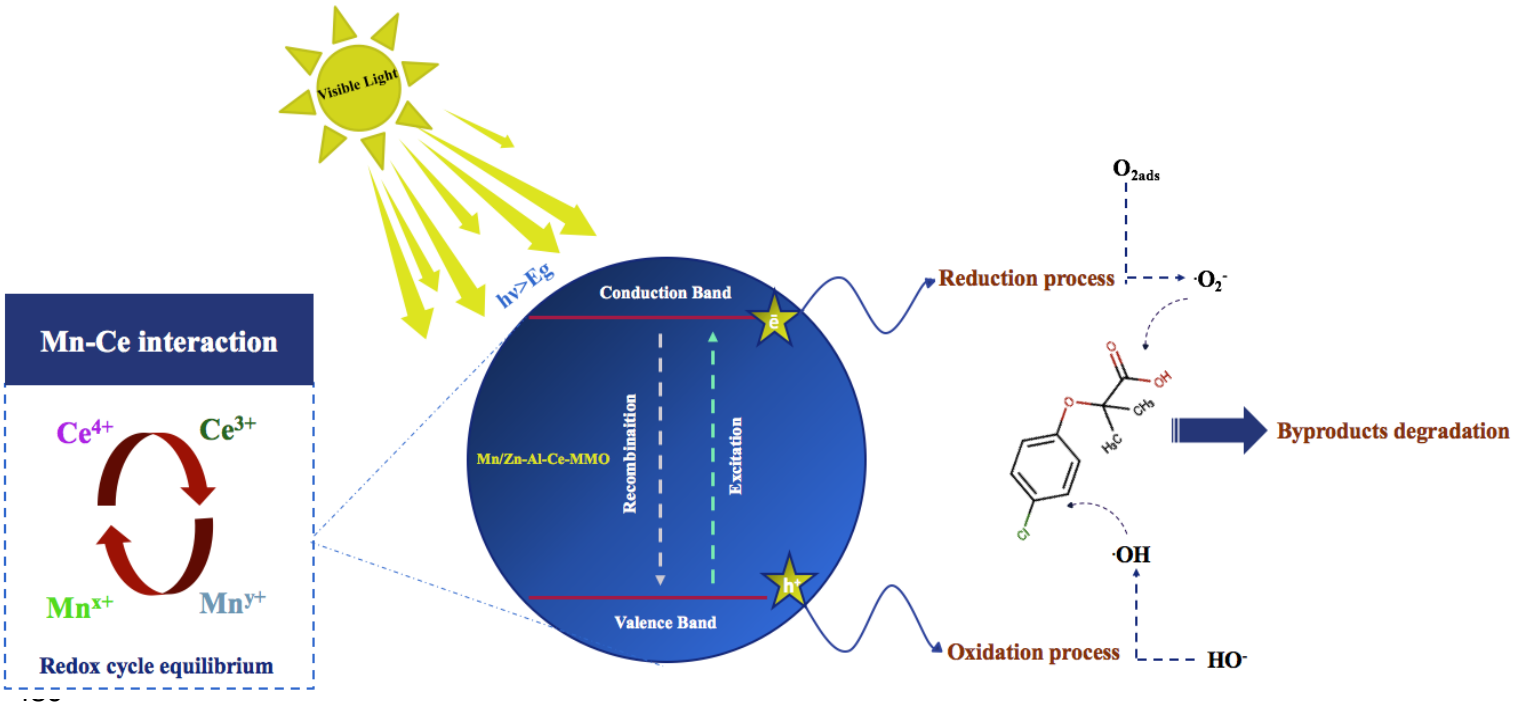

Fig.12. Schematic illustration of the photocatalyst surface under light irradiation.

3.2.4. Photostability and reusability of catalyst

The stability and the recyclability application of the used catalyst are shown in Fig.12. The result depicted that the photocatalytic activity of Mn_3O_4/ZnO-Al_2O_3-CeO_2 catalyst remained almost stable even at 3 cycles with a low reduction of degradation efficiency from 93 to 74%, which can be due to the mass loss of the catalyst. The present study demonstrates that Mn_3O_4/ZnO-Al_2O_3-CeO_2 present an excellent stability and photocatalytic activity and can be used like promising catalyst for several time for the degradation of emergent pollutant. The obtained results indicate that this efficient and stable system could be considered as a potential catalyst and presents a trend practical application in photocatalytic degradation process of emergent molecules.

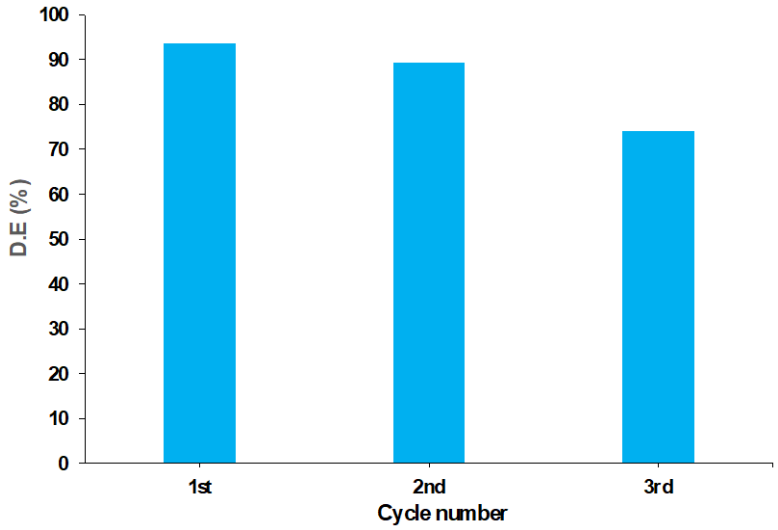

Fig.12. Reusability and photostability of Mn_3O_4/ZnO-Al_2O_3-CeO_2.

Conclusion

In the present study, a well-shaped heterostructure was obtained by doping pristine Zn-(Al/Ce)-LDHs with Mn in reasonable content of 3% and calcination treatment at 500°C. A thorough optoelectronic properties analysis suggests that the high visible absorption capacity of the catalyst is linked to the presence of Mn^{2+} and Mn^{3+} in the catalyst system. Mn_3O_4/ ZnO-Al_2O_3-CeO_2 mixed oxides obtained with abundance particles size less than 30 nm and with an efficient absorption capacity in both ultraviolet and visible regions, which shows a small band gap (2.34 eV). The corresponding catalyst outperforms the others with regard of photocatalytic performance activity when under visible light. This catalyst exhibits an excellent photocatalytic performance toward CA under visible light irradiation, which achieved 93.6 % for 50 mg/L of CA by using a low catalyst dose of 20 mg/L. In conclusion, charge transfer between Mn^{x+}, Ce^{3+}, and Ce^{4+} is the main reason for the significant separation between the photogenerated electrons and holes. So, the ability to produce Mn and Ce in different oxidation states with strong interaction and synergy between Ce and Mn redox couples improves photocatalytic performance under combined and simultaneous action. According to the reusability tests, the catalyst is much more photostable under visible light irradiation. This study could offer a straightforward method for the synthesis of a cost-effective photocatalyst based on mixed oxides of Mn_3O_4/ZnO-Al_2O_3-CeO_2 derived from LDHs stricture thus enable their application in environmental pollution control issues.

Acknowledgment

The authors would like to thank the National Center for Scientific and Technical Research (CNRST) of Morocco for microscopic analysis performed in their technical facilities. The authors also acknowledge the financial support through Researchers Supporting Project number (RSPD2024R768), King Saud University, Riyadh, Saudi Arabia.

Declarations

Funding

Researchers Supporting Project number (RSPD2024R768), King Saud University, Riyadh, Saudi Arabia

Competing interests

The authors have no relevant financial or non-financial interests to disclose

Author Contributions

Fatima Zahra Janani: Performed the experiments; Analyzed and interpreted the data, Writing: original draft. **Habiba Khiar:** Performed the experiments; Analyzed and interpreted the data. **Nawal Taoufik:** Analyzed and interpreted the data; Data curation. **Mhamed Sadiq:** Analyzed and interpreted the data; Data curation. **Lidia Favier:** Analyzed and interpreted the data; Writing: review and editing, Data curation. **Abdelrahman Osama Ezzat:** Writing: review and editing. **Alaâeddine Elhalil:** Analyzed and interpreted the data; Writing: review and editing. **Noureddine Barka:** Conceived and designed the experiments; Analyzed and interpreted the data; Writing: review and editing, Supervision.

Ethics approval and consent to participate

Not applicable.

Consent for publication

Not applicable

Availability of data and materials

The datasets used and/or analyzed during this study are available from the corresponding author on reasonable request.

References

Abdi M, Mahdikhah V, Sheibani S (2020) Visible light photocatalytic performance of La-Fe co-doped SrTiO3 perovskite powder. Opt Mater (Amst) 102:109803. https://doi.org/10.1016/j.optmat.2020.109803

Ajala OJ, Tijani JO, Salau RB, et al (2022) A review of emerging micro-pollutants in hospital wastewater: Environmental fate and remediation options. Results Eng 16:100671. https://doi.org/10.1016/j.rineng.2022.100671

Akir S, Hamdi A, Addad A, et al (2017) Facile synthesis of carbon-ZnO nanocomposite with enhanced visible light photocatalytic performance. Appl Surf Sci 400:461–470. https://doi.org/10.1016/j.apsusc.2016.12.212

Aydın S, Ulvi A, Bedük F, Aydın ME (2022) Pharmaceutical residues in digested sewage sludge: Occurrence, seasonal variation and risk assessment for soil. Sci Total Environ 817:. https://doi.org/10.1016/j.scitotenv.2021.152864

Beausse J (2004) Selected drugs in solid matrices: A review of environmental determination, occurrence and properties of principal substances. TrAC - Trends Anal Chem 23:753–761. https://doi.org/10.1016/j.trac.2004.08.005

Binas V, Stefanopoulos V, Kiriakidis G, Papagiannakopoulos P (2019) Photocatalytic oxidation of gaseous benzene, toluene and xylene under UV and visible irradiation over Mn-doped TiO2 nanoparticles. J Mater 5:56–65. https://doi.org/10.1016/j.jmat.2018.12.003

Cerrato E, Calza P, Cristina Paganini M (2022) Photocatalytic reductive and oxidative ability study of pristine ZnO and CeO2-ZnO heterojunction impregnated with Cu2O. J Photochem Photobiol A Chem 427:113775. https://doi.org/10.1016/j.jphotochem.2022.113775

Chafi S, Azzouz A, Ballesteros E (2022) Occurrence and distribution of endocrine disrupting chemicals and pharmaceuticals in the river Bouregreg (Rabat, Morocco). Chemosphere 287:132202. https://doi.org/10.1016/j.chemosphere.2021.132202

Chen P, Wang F, Zhang Q, et al (2017) Photocatalytic degradation of clofibric acid by g-C3N4/P25 composites under simulated sunlight irradiation: The significant effects of reactive species. Chemosphere 172:193–200. https://doi.org/10.1016/j.chemosphere.2017.01.015

Cheng G, Yuan C, Ruan W, et al (2023) Visible light enhanced persulfate activation for degradation of tetracycline via boosting adsorption of persulfate by ligand-deficient MIL-101(Fe) icosahedron. Chemosphere 317:137857. https://doi.org/10.1016/j.chemosphere.2023.137857

Dias JA, Gualdi AJ, Costa LJD, et al (2020) Effects of bismuth/lanthanum-substitution on optical, dielectric and magnetic properties of bismuth–iron titanate. Mater Today Commun

24:101193. https://doi.org/10.1016/j.mtcomm.2020.101193

Elhalil A, Elmoubarki R, Farnane M, et al (2018a) Synthesis, characterization and efficient photocatalytic activity of novel Ca/ ZnO-Al2O3 nanomaterial. Mater Today Commun 16:194–203. https://doi.org/10.1016/j.mtcomm.2018.06.005

Elhalil A, Elmoubarki R, Farnane M, et al (2018b) Photocatalytic degradation of caffeine as a model pharmaceutical pollutant on Mg doped ZnO-Al2O3 heterostructure. Environ Nanotechnology, Monit Manag 10:63–72. https://doi.org/10.1016/j.enmm.2018.02.002

Favier L, Rusu L, Simion AI, et al (2019) EFFICIENT DEGRADATION OF CLOFIBRIC ACID BY HETEROGENEOUS PHOTOCATALYTIC OXIDATION PROCESS. 18:1683–1692

Hussain MM, Rahman MM, Asiri AM (2016) Efficient 2-nitrophenol chemical sensor development based on Ce2O3 nanoparticles decorated cnt nanocomposites for environmental safety. PLoS One 11:1–17. https://doi.org/10.1371/journal.pone.0166265

Ighalo JO, Ajala OJ, Umenweke G, et al (2020) Mitigation of clofibric acid pollution by adsorption: A review of recent developments. J Environ Chem Eng 8:. https://doi.org/10.1016/j.jece.2020.104264

Iqbal J, Shah NS, Khan ZUH, et al (2022) Visible light driven doped CeO2 for the treatment of pharmaceuticals in wastewater: A review. J Water Process Eng 49:103130. https://doi.org/10.1016/j.jwpe.2022.103130

Janani FZ, Khiar H, Taoufik N, et al (2021) ZnO–Al2O3–CeO2–Ce2O3 mixed metal oxides as a promising photocatalyst for methyl orange photocatalytic degradation. Mater Today Chem 21:. https://doi.org/10.1016/j.mtchem.2021.100495

Janani FZ, Khiar H, Taoufik N, et al (2022) ZnO-Zn2TiO4 heterostructure for highly efficient photocatalytic degradation of pharmaceuticals. Environ Sci Pollut Res. https://doi.org/10.1007/s11356-022-22791-6

Kijlstra WS, Poels EK, Bliek A, et al (1997) Characterization of Al2O3-supported manganese oxides by electron spin resonance and diffuse reflectance spectroscopy. J Phys Chem B 101:309–316. https://doi.org/10.1021/jp962343i

Korkmaz NE, Savun-Hekimoğlu B, Aksu A, et al (2022) Occurrence, sources and environmental risk assessment of pharmaceuticals in the Sea of Marmara, Turkey. Sci Total Environ 819:. https://doi.org/10.1016/j.scitotenv.2022.152996

Liang X, Wang P, Gao Y, et al (2020) Design and synthesis of porous M-ZnO/CeO2 microspheres as efficient plasmonic photocatalysts for nonpolar gaseous molecules oxidation: Insight into the role of oxygen vacancy defects and M=Ag, Au nanoparticles. Appl Catal B Environ 260:118151. https://doi.org/10.1016/j.apcatb.2019.118151

607 Lin H, Tang X, Wang J, et al (2021) Enhanced visible-light photocatalysis of clofibric acid using
608 graphitic carbon nitride modified by cerium oxide nanoparticles. J Hazard Mater 405:124204.
609 https://doi.org/10.1016/j.jhazmat.2020.124204

610 Ma B, Liu Z, Wang L, et al (2024) Significantly boosting photocatalytic degradation efficiency
611 through simple Br modification. Mater Sci Semicond Process 169:107941.
612 https://doi.org/10.1016/j.mssp.2023.107941

613 Mohan R, Krishnamoorthy K, Kim SJ (2012) Enhanced photocatalytic activity of Cu-doped ZnO
614 nanorods. Solid State Commun 152:375–380. https://doi.org/10.1016/j.ssc.2011.12.008

615 Morales-mendoza G, Tzompantzi F, García-mendoza C, et al (2015) Mn-doped Zn / Al layered
616 double hydroxides as photocatalysts for the 4-chlorophenol photodegradation. Appl Clay Sci
617 118:38–47. https://doi.org/10.1016/j.clay.2015.08.030

618 Nagendran S, Periyasamy G, Kamath PV (2018) Hydration-induced interpolytype transformations
619 in the bayerite-derived nitrate-intercalated layered double hydroxide of Li and Al. J Solid
620 State Chem 266:226–232. https://doi.org/10.1016/j.jssc.2018.07.016

621 Olfs HW, Torres-Dorante LO, Eckelt R, Kosslick H (2009) Comparison of different synthesis
622 routes for Mg-Al layered double hydroxides (LDH): Characterization of the structural phases
623 and anion exchange properties. Appl Clay Sci 43:459–464.
624 https://doi.org/10.1016/j.clay.2008.10.009

625 Pratt GW, Coelho R (1959) Optical absorption of CoO and MnO above and below the Néel
626 temperature. Phys Rev 116:281–286. https://doi.org/10.1103/PhysRev.116.281

627 Rebelo D, Correia AT, Nunes B (2020) Acute and chronic effects of environmental realistic
628 concentrations of clofibric acid in Danio rerio: Behaviour, oxidative stress, biotransformation
629 and lipid peroxidation endpoints. Environ Toxicol Pharmacol 80:103468.
630 https://doi.org/10.1016/j.etap.2020.103468

631 Reza RA, Ahmaruzzaman M, Sil AK, Gupta VK (2014) Comparative adsorption behavior of
632 ibuprofen and clofibric acid onto microwave assisted activated bamboo waste. Ind Eng Chem
633 Res 53:9331–9339. https://doi.org/10.1021/ie404162p

634 Sahoo GP, Samanta S, Bhui DK, et al (2015) Hydrothermal synthesis of hexagonal ZnO
635 microstructures in HPMC polymer matrix and their catalytic activities. J Mol Liq 212:665–
636 670. https://doi.org/10.1016/j.molliq.2015.10.019

637 Sescu AM, Harja M, Favier L, et al (2020) Zn/la mixed oxides prepared by coprecipitation:
638 Synthesis, characterization and photocatalytic studies. Materials (Basel) 13:1–19.
639 https://doi.org/10.3390/ma13214916

640 Shan K, Zhai F, Yi ZZ, et al (2021) Mixed conductivity and the conduction mechanism of the

orthorhombic CaZrO3 based materials. Surfaces and Interfaces 23:100905. https://doi.org/10.1016/j.surfin.2020.100905

Shang K, Li W, Wang X, et al (2019) Degradation of p-nitrophenol by DBD plasma/Fe2+/persulfate oxidation process. Sep Purif Technol 218:106–112. https://doi.org/10.1016/j.seppur.2019.02.046

Shehu Z, Nyakairu GWA, Tebandeke E, Odume ON (2022) Overview of African water resources contamination by contaminants of emerging concern. Sci Total Environ 852:158303. https://doi.org/10.1016/j.scitotenv.2022.158303

Shi Y, Geng J, Li X, et al (2022) Effects of DOM characteristics from real wastewater on the degradation of pharmaceutically active compounds by the UV/H2O2 process. J Environ Sci (China) 116:220–228. https://doi.org/10.1016/j.jes.2021.12.017

Silori R, Shrivastava V, Singh A, et al (2022) Global groundwater vulnerability for Pharmaceutical and Personal care products (PPCPs): The scenario of second decade of 21st century. J Environ Manage 320:115703. https://doi.org/10.1016/j.jenvman.2022.115703

Taoufik N, Boumya W, Elmoubarki R, et al (2022) Experimental design, machine learning approaches for the optimization and modeling of caffeine adsorption. Mater Today Chem 23:. https://doi.org/10.1016/j.mtchem.2021.100732

Velu S, Shah N, Jyothi TM, Sivasanker S (1999) Effect of manganese substitution on the physicochemical properties and catalytic toluene oxidation activities of Mg-Al layered double hydroxides. Microporous Mesoporous Mater 33:61–75. https://doi.org/10.1016/S1387-1811(99)00123-7

Wan J, Tao F, Shi Y, et al (2022) Designed preparation of nano rod shaped CeO2-MnOx catalysts with different Ce/Mn ratios and its highly efficient catalytic performance for chlorobenzene complete oxidation: New insights into structure–activity correlations. Chem Eng J 433:133788. https://doi.org/10.1016/j.cej.2021.133788

Wang Y, He X, Gao P, et al (2024) Enhanced photocatalytic gaseous formaldehyde degradation using N-CQDs/OVs-TiO2 composite under visible light: Unraveling the synergistic effects of N-CQDs and oxygen vacancies. Environ Res 247:118301. https://doi.org/10.1016/j.envres.2024.118301

Wu C, Shen L, Zhang YC, Huang Q (2011) Solvothermal synthesis of Cr-doped ZnO nanowires with visible light-driven photocatalytic activity. Mater Lett 65:1794–1796. https://doi.org/10.1016/j.matlet.2011.03.070

Wu S, Wang Z, Wan L, et al (2022) Electrocatalytic hydrodechlorination of clofibric acid (CA) using Pd/Ni foam electrodes: The effects of Ni(OH)2 and complexing agents on electrode preparation. J Electroanal Chem 915:116358.

https://doi.org/10.1016/j.jelechem.2022.116358

Yang ZM, Huang GF, Huang WQ, et al (2014) Novel Ag3PO4/CeO2 composite with high efficiency and stability for photocatalytic applications. J Mater Chem A 2:1750–1756. https://doi.org/10.1039/c3ta14286h

ZHANG L, DAI C hua, ZHANG X xiu, et al (2016) Synthesis and highly efficient photocatalytic activity of mixed oxides derived from ZnNiAl layered double hydroxides. Trans Nonferrous Met Soc China (English Ed 26:2380–2389. https://doi.org/10.1016/S1003-6326(16)64360-1

Zhao Q, Liu Q, Han J, et al (2019) The effect of cerium incorporation on the catalytic performance of cobalt and manganese containing layer double oxides for acetone oxidation. J Chem Technol Biotechnol 94:3753–3762. https://doi.org/10.1002/jctb.5868

Chaudhari S M, Gonsalves O S, Nemade P R (2021) Enhanced photocatalytic degradation of Diclofenac with Agl/CeO2: A comparison with Mn, Cu and Ag-doped CeO2. Mater Resear Bull 143: 111463. https://doi.org/10.1016/j.materresbull.2021.111463

Favier L, Rusu L, Simion A I, Hlihor R M, Pacala M L, Augustyniak A (2019) efficient degradation of clofibric acid by heterogeneous photocatalytic oxidation process. Environmental Engineering and Management Journal 18(8): 1683-1692.